Journal of
Synchrotron
Radiation

ISSN 0909-0495

Received 2 February 2012
Accepted 24 May 2012

In situ three-dimensional reciprocal-space mapping during mechanical deformation

T. W. Cornelius,[a,b]* A. Davydok,[c] V. L. R. Jacques,[d] R. Grifone,[e] T. Schülli,[d] M.-I. Richard,[a,b] G. Beutier,[e] M. Verdier,[e] T. H. Metzger,[f] U. Pietsch[c] and O. Thomas[a,b]

[a]Aix-Marseille University, IM2NP, Faculté des Sciences et Techniques, Campus de Saint-Jérôme, Avenue Escadrille Normandie Niemen, Case 142, F-13397 Marseille Cedex, France, [b]CNRS, IM2NP (UMR 7334), Faculté des Sciences et Techniques, Campus de Saint-Jérôme, Avenue Escadrille Normandie Niemen, Case 142, F-13397 Marseille Cedex, France, [c]University of Siegen, Festkörperphysik, Walter-Flex-Strasse 3, D-57072 Siegen, Germany, [d]European Synchrotron Radiation Facility, 6 rue Jules Horowitz, BP 220, F-38043 Grenoble Cedex, France, [e]SIMaP, Grenoble Institute of Technology and CNRS, BP 75, F-38402 Saint-Martin d'Hères Cedex, France, and [f]Max Planck Institute of Colloids and Interfaces, Department of Biomaterials, D-14424 Potsdam, Germany. E-mail: thomas.cornelius@im2np.fr

Mechanical deformation of a SiGe island epitaxically grown on Si(001) was studied by a specially adapted atomic force microscope and nanofocused X-ray diffraction. The deformation was monitored during *in situ* mechanical loading by recording three-dimensional reciprocal-space maps around a selected Bragg peak. Scanning the energy of the incident beam instead of rocking the sample allowed the safe and reliable measurement of the reciprocal-space maps without removal of the mechanical load. The crystal truncation rods originating from the island side facets rotate to steeper angles with increasing mechanical load. Simulations of the displacement field and the intensity distribution, based on the finite-element method, reveal that the change in orientation of the side facets of about 25° corresponds to an applied pressure of 2–3 GPa on the island top plane.

Keywords: X-ray diffraction; nanofocused XRD; energy scan; 3D reciprocal-space mapping; mechanical deformation/properties; *in situ* AFM.

1. Introduction

In the recent past, low-dimensional materials have attracted enormous attention owing to size effects originating from the spatial confinement which allows tailoring their properties such as the electronic density of states, band structure, phonon dispersion and mechanical properties in general. Concerning the mechanical properties of nano-objects, the plastic behavior has mainly been explored. In the plastic regime the object can be investigated before and after compression and thus detailed studies are available mostly on metals revealing a trend that 'smaller is stronger' for structures with sizes in the micrometer range (Uchic *et al.*, 2004). More recently, the mechanical behavior of semiconductor submicrometer structures such as GaAs (Michler *et al.*, 2007) or Si (Östlund *et al.*, 2009) has been studied. Owing to deep Peierls valleys, semiconductors are brittle at room temperature; surprisingly, this is no longer true at this length scale: small-diameter (few hundred nanometers) semiconductor pillars exhibit ductile behavior instead (Michler *et al.*, 2007; Östlund *et al.*, 2009). Although small structures are expected to display bulk elasticity down to sizes of a few nanometers, conflicting results are found in the literature concerning their elastic properties. This points out the difficulty in developing tools that can reliably apply and measure a very small force on a nano-object and detect its change in size simultaneously. The Young modulus of single nanowires has been investigated either by oscillating the wires and measuring their resonance frequency or by contact atomic force microscopy (AFM) (Smith *et al.*, 2008; Cimalla *et al.*, 2008; Wang *et al.*, 2001; Chen *et al.*, 2006; Jing *et al.*, 2006; Ngo *et al.*, 2006; Heidelberg *et al.*, 2006). In these studies contradictory results were reported on the size dependence of the elastic properties attributed to the wire processing or to oxidation leading to core-shell structures. Thus, additional studies, in particular *in situ* measurements, are mandatory in order to shed more light on the influence of size effects as well as contamination on the mechanical response of nanostructures. In the recent past, *in situ* techniques have been developed employing μLaue diffraction (Kirchlechner *et al.*, 2011; Maaß *et al.*, 2007, 2008) and Raman spectroscopy (Lee *et al.*, 2007), as well as scanning electron microscopy (Richter *et al.*, 2009; Kiener *et al.*, 2008). These *in situ* methods are

appropriate for observing the propagation of deformation of the specimen during mechanical testing.

In this work we demonstrate a method to directly probe the mechanical response (elastic and plastic) in an individual structure by the change of its crystal lattice by local X-ray diffraction under mechanical load. Using highly focused X-rays in combination with a specially adapted *in situ* AFM constitutes an experimental apparatus that can apply a local force to a nano-object and detect the resulting deformation independently. As presented by Scheler *et al.* (2009), the *in situ* AFM is used to image, select and deform a nanostructure of choice. Simultaneously to the compression of the selected object, X-ray diffraction patterns were recorded by a two-dimensional detector. This combination allowed us to determine the Young modulus of single SiGe islands (Rodrigues *et al.*, 2009). However, a two-dimensional X-ray diffraction image only provides one specific cut through the three-dimensional reciprocal-space intensity produced by a nanoscale structure. Moreover, during compression the Bragg peak moves out of the detector plane owing to the change of the interatomic distances. In order to fully record the induced structural change during deformation, it is necessary to measure *in situ* the complete three-dimensional intensity distribution of the Bragg reflection coming from the nanostructure under investigation. Unfortunately, this is impossible using a two-dimensional detector and monochromatic radiation, as long as the three-dimensional reciprocal-space maps (3D-RSMs) are recorded by subsequent rocking curves taken at different angles of incidence (Fewster, 1997). In that case, any movement of diffractometer motors induces vibrations damaging the AFM tip and/or the nano-object during compression. Alternatively, the X-ray energy can be varied in a pre-determined range which allows mapping the reciprocal space in three dimensions (Cornelius *et al.*, 2011). Here, this technique is applied in order to investigate the strain induced in SiGe islands by mechanical loading.

2. Experimental

The sample investigated is a SiGe island grown by liquid phase epitaxy on Si(001). The Ge content of 12% in the island results in a lattice expansion of 0.5% with respect to pure Si. The epitaxial relationship leads to a tensile strain in the island along the vertical direction. The Ge content also pre-determines the island size (Dorsch *et al.*, 1998). A scanning electron microscopy image of such islands is presented in Fig. 1, showing the shape of a truncated pyramid [with four (111) side facets] with a square base width of 1 µm, a height of 500 nm, and the top facet with a side length of about 300 nm.

X-ray diffraction experiments have been performed at the ID01 beamline of the European Synchrotron Radiation Facility (ESRF) in Grenoble, France. A photon energy of 9 keV ($\lambda = 0.138$ nm) was selected employing a double-bounce channel-cut Si(111) monochromator. The X-ray beam was focused using a Fresnel zone plate (FZP) with a diameter of $D = 200$ µm and an outermost zone width of $\Delta = 70$ nm. Such FZPs are conventionally fabricated by electron beam lithography or by holographic techniques (Jefimovs *et al.*, 2007; Sarkar *et al.*, 2010). They are routinely employed nowadays for nanodiffraction and coherent diffraction imaging experiments on single nanowires (Favre-Nicolin *et al.*, 2010), nanorods (Biermanns *et al.*, 2009), nano-crystals (Robinson & Harder, 2009), *etc*.

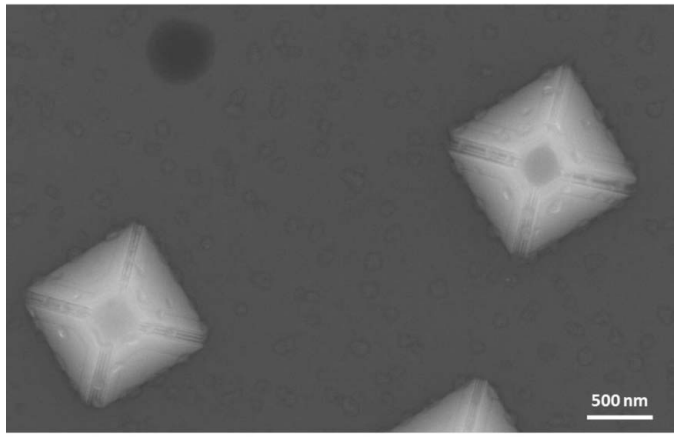

Figure 1
Scanning electron microscopy image of SiGe islands epitaxically grown on Si(001).

The outermost zone of a FZP is of the same order as the diffraction-limited focal spot size ($1.22\Delta \simeq 85$ nm) that can be obtained with the FZP. The experimentally obtained focal size amounts to 200 nm and 300 nm (full width at half-maximum) in the vertical and horizontal direction, respectively. The broadening of the focus compared with the diffraction-limited value is probably caused by vibrations. The focal spot of the X-ray beam is thus smaller than the SiGe island. The diffracted X-rays were recorded by a MAXIPIX two-dimensional pixel detector with a pixel size of 55 µm × 55 µm mounted 1.35 m after the sample. The experimental set-up is schematically shown in Fig. 2.

The FZP is a chromatic focusing optics, *i.e.* the focal distance f is a function of the X-ray energy: $f = D\Delta E/(hc)$. The focal depth of the fully (200 µm × 200 µm) illuminated FZP amounts to 0.29 mm. This focal depth is increased when

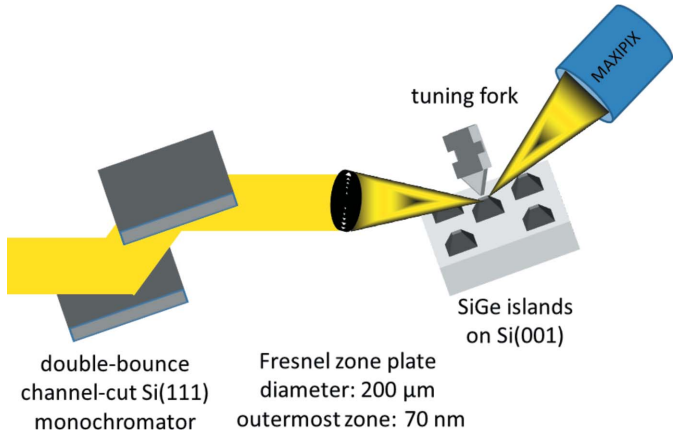

Figure 2
Schematic of the experimental set-up.

reducing the illuminated area of the FZP (Mastropietro *et al.*, 2011) and, thus, the energy of the incident X-ray beam may be changed within a wider range without deteriorating the focal spot on the structure under investigation. For a fully illuminated FZP the X-ray energy may be varied only by ∼30 eV. In this experiment the illumination area was set to be 50 µm × 50 µm which results in a focal depth of about 1.5 mm and, hence, the energy may be varied within 150 eV without losing the focal spot on the sample. The reduction of the illuminated area on the FZP also reduces the numerical aperture (NA) of the focusing optics from 2×10^{-3} to 5×10^{-4}. This results in an increase of the minimum spot size accordingly as it is limited by λ/NA. Here, the limit amounts to 280 nm. As the parameters defining our minimum spot size result from other sources (such as vibrations), the effect of the reduced aperture on the focal size is negligible. In addition, the beam divergence decreases from 0.11 to 0.028° when reducing the illumination area of the FZP.

The *in situ* AFM was installed on a cradle allowing for its positioning at any Bragg angle. A quartz tuning fork was employed as AFM force sensor and a tungsten tip was glued on one of the tuning fork prongs (Rodrigues *et al.*, 2008). For *in situ* compression tests the AFM tip was electrochemically blunted to a radius of curvature of the order of 1–2 µm. Although the AFM tip is not shaped to grant a homogeneous pressure application (like for a flat punch), we do not consider any shape dependence for further data treatment. The sample and the AFM tip were aligned separately with respect to the nanofocused X-ray beam. A scanning X-ray diffraction map (SXDM; Mocuta *et al.*, 2008) of the sample and a scanning absorption image of the AFM tip at the symmetric Si(004) Bragg angle are presented in Figs. 3(*a*) and 3(*b*), respectively. The SXDM shows the arrangement of the SiGe islands on the Si(001) surface. The clear separation of neighboring structures enables us to illuminate a single individual island with the nanofocused X-ray beam. When scanning the AFM tip through the X-ray focus under diffraction conditions, the tip may either block the incident beam or the beam diffracted by the sample. Thus, two shadows of the AFM tip are visible in the absorption image. In Fig. 3(*b*) the lower shadow originates from the absorption of the incident beam while the upper one is caused by the absorption of the diffracted X-rays. This scanning absorption image was recorded while the AFM tip was a few micrometers above the sample surface. By geometrical consideration, we deduce that the X-ray beam *and* the AFM tip will hit the sample at the *same* position on the sample surface in the point between the two shadows marked by a cross in Fig. 3(*b*). This allows a precise alignment of the island with respect to both the AFM tip and the X-ray beam. It also allows for determining the radius of curvature of the blunted AFM tip. After deconvolution with the X-ray beam size it is estimated to be 1.5–2 µm. The mutual alignment of the X-ray beam, the SiGe island and the AFM tip is achieved with an accuracy of the order of the X-ray focal spot. Here, additional scattering of the X-rays has to be considered when the AFM tip is illuminated by the synchrotron beam and, thus, it allows for an *in situ* verification of the alignment.

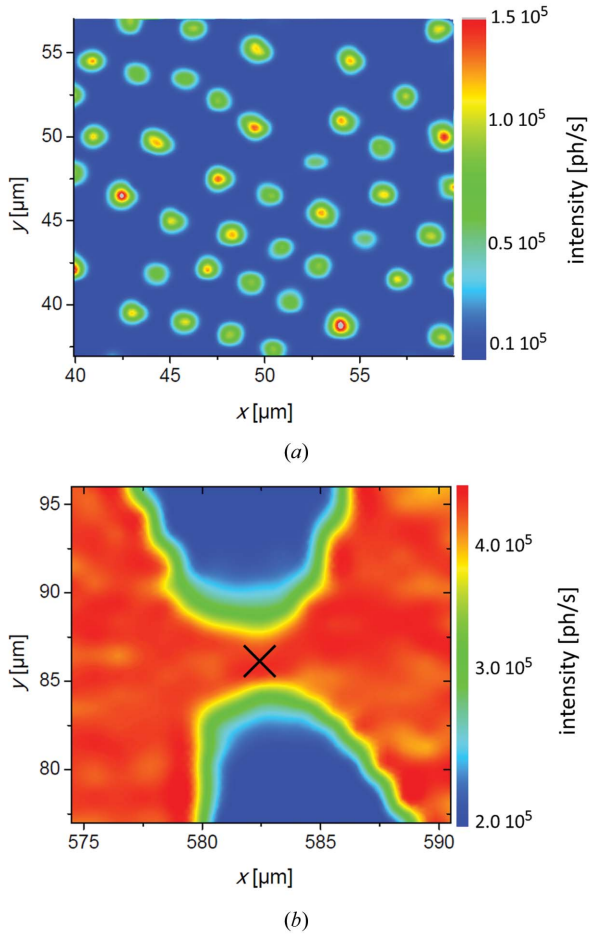

Figure 3
(*a*) Scanning X-ray diffraction map of a SiGe island array and (*b*) a scanning absorption image of the AFM tip at the SiGe(004) Bragg angle. The cross in (*b*) marks the position of the focal spot of the X-ray beam.

3. Results and discussion

3.1. Experiment

After alignment, the AFM tip is brought into contact with the selected island and moved down consecutively to increase the force applied on the structure. Owing to the simultaneous deformations of the whole system given by sample, AFM tip and tuning fork, the applied force cannot be directly determined from the AFM tip displacement. It can be indirectly inferred from a shift of the resonance frequency of the quartz tuning fork employing the Hertz contact model (Rodrigues *et al.*, 2009).

To measure three-dimensional reciprocal-space maps during the deformation, energy scans are performed. In this aim, the energy is varied by $\Delta E = \pm 100$ eV (corresponding to $\Delta q = \pm 0.516$ nm^{-1} as obtained by a θ–2θ scan in the range $\Delta\theta = \pm 0.37°$) in steps of 1 eV. The exposure time amounted to 10 s at each energy step. Owing to the alignment of the undulator gap at each energy a complete energy scan lasted for about 1 h. Despite the long measurement time, no drifts, neither of the X-ray beam nor of the AFM, were observed, *i.e.* two subsequent energy scans at the same compression state revealed the same diffraction signal. This also implies that the

radiation damage is negligible. Fig. 4 displays two-dimensional diffraction patterns (first line), the reconstructed three-dimensional reciprocal-space maps (middle), and (q_x, q_z) cuts through the 3D-RSMs (bottom) at $q_y = 0$ for a SiGe island at different deformation stages. The data show the Si(004) Bragg reflection at $q_z = 46.3$ nm^{-1}, the crystal truncation rod (CTR) of the Si substrate, and the signal of the SiGe island ($q_z = 46.05$ nm^{-1}) including the CTRs originating from the side facets of the island. The positions of the Si(004) Bragg reflection and the signal of the SiGe island are indicated by dashed lines. In the central vertical cuts the island facet CTRs are highlighted by dotted lines. During pressure application on the island top facet the substrate CTR on the two-dimensional diffraction patterns remains at the same position proving that the whole sample does not tilt during the experiment. Thus, all changes revealed by the *in situ* three-dimensional diffraction mapping originate from the deformation of the specimen. Comparing with the diffraction pattern of the virgin sample (Fig. 4*a*), the central part of the diffraction signal of the SiGe island vanishes with increasing mechanical load [see Figs. 4(*b*) and 4(*c*)], while the Si(004) Bragg reflection becomes more diffuse. Hence, a part of the island signal becomes superimposed with the substrate Bragg peak. In addition, the Si(004) Bragg peak develops a substructure for increasing load which may be caused by a superposition with the SiGe island signal or by strain induced in the Si substrate. As visible in Figs. 4(*b*) and 4(*c*), the streaks originating from the island side facets turn to steeper angles with increasing load. The load is expressed here by the vertical movement of the AFM tip against the island top facet after reaching contact although the applied pressure cannot be determined directly from this movement. Following the direction of enhanced intensity along the contours of the triangular intensity distribution (see dotted lines in Fig. 4), the angle of elevation with respect to [110] of the pristine sample is estimated to be $36 \pm 2^\circ$, being in good agreement with the expected 35.26° angle between [110]

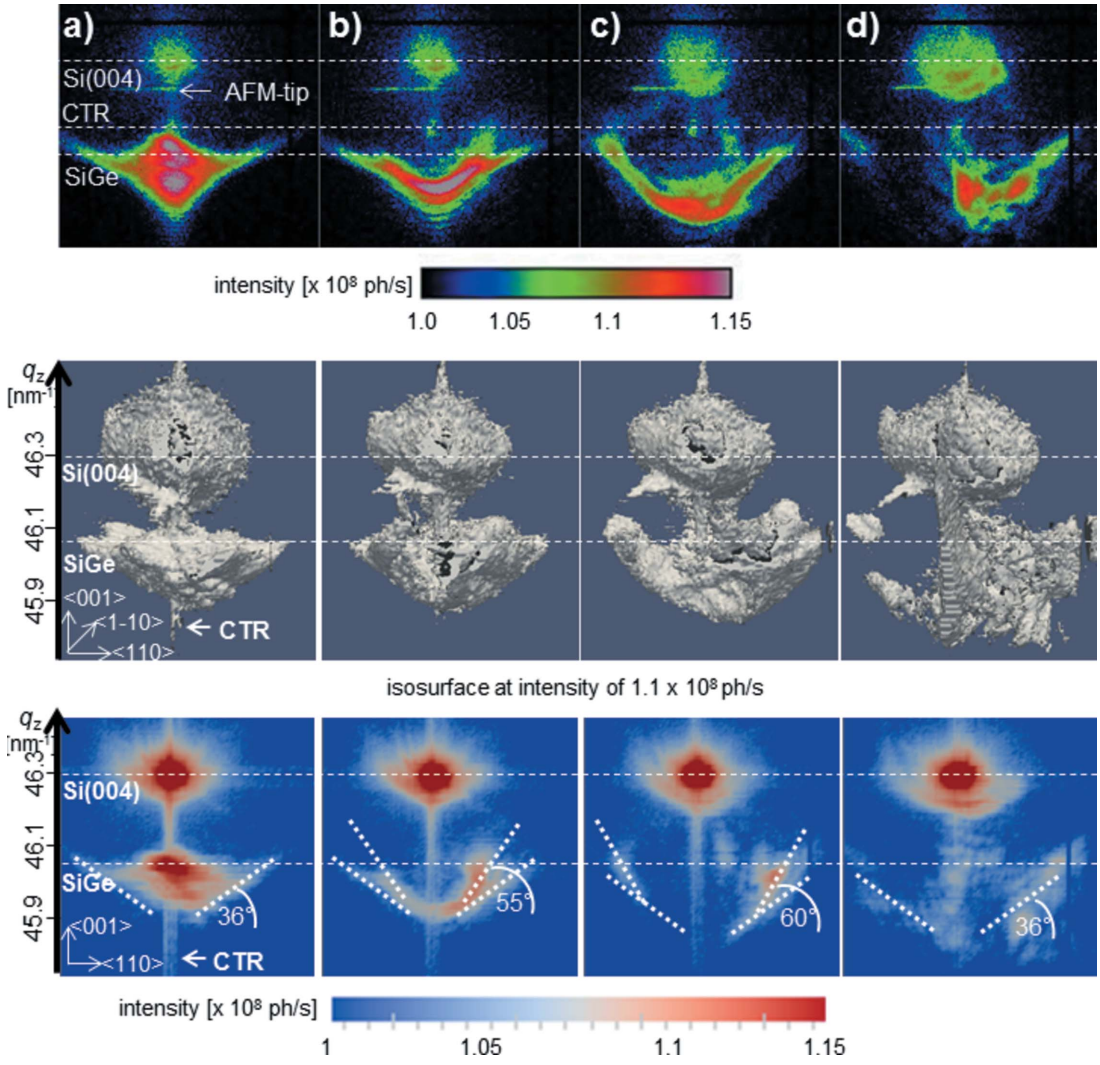

Figure 4
Two-dimensional X-ray diffraction patterns (upper row), reconstructed three-dimensional reciprocal-space maps (central row), and (q_x, q_z) cuts through the *in situ* 3D-RSMs at central q_y (lower row) for (*a*) a pristine SiGe island and (*b*)–(*d*) the same SiGe island at different deformation stages. The position of the Si(004) Bragg reflection and the signal of the SiGe island is indicated by dashed lines. The dotted lines highlight the CTRs originating from the island side facets.

and [111]. The appearance of (111) side facets has been determined for these islands by high-resolution X-ray diffraction (Wiebach *et al.*, 2000). This angle increases to 55 ± 2° and to 60 ± 2° when moving the AFM tip 470 nm and 750 nm downwards, respectively. The increasing angles of the CTRs indicate that the island shape is being deformed during the mechanical loading. In the stage of highest loading [see Fig. 4(*d*)] when the AFM tip has been lowered by 1190 nm the CTR angle returns back to 36 ± 2° as found for the pristine sample accompanied by a vanishing of a clear island signal. In addition, speckle patterns are observed around the position of the SiGe island signal and along the substrate CTR which may indicate the presence of defects. This finding cannot be clearly interpreted. The most probable explanation is a fracture of the central part of the islands into several pieces accompanied by strain release of the remaining outer parts, bringing the side planes back to their initial position found before the compression. This hypothesis could not be verified after loading owing to a backlash of the AFM tip during retraction which first increased the load before releasing the pressure.

3.2. FEM simulations

For a deeper understanding of the experimental results, the displacement field and the shear stress of a SiGe island with a base width of 1 μm and a height of 500 nm epitaxically grown on Si(001) was simulated by the finite-element method (FEM) using COMSOL's *Multiphysics* code. The lattice mismatch between the Si substrate and the $Si_{88}Ge_{12}$ island was simulated in the framework of thermoelasticity. The temperature was taken to be constant, and island and substrate were assigned different thermal-expansion coefficients (Christansen *et al.*, 1994; Benabbas *et al.*, 1996). For calculations, the complete elastic stiffness tensor was taken into account. The stiffness for the SiGe island was derived employing Vegard's law (Rodrigues *et al.*, 2009; Wortman & Evans, 1965; Vegard, 1921). For the sake of simplification we treated the islands as a homogeneous solid solution neglecting the inhomogeneous Ge composition as determined by high-resolution X-ray diffraction analysis (Wiebach *et al.*, 2000). For computations of the island deformation a distributed load on the island top facet was used. The corresponding three-dimensional reciprocal-space maps were obtained by fast Fourier transformation (FFT) (Takagi, 1969). For this purpose, first the phase is calculated which originates from the displacement field in the sample with respect to the Si reference lattice. From this phase the three-dimensional FFT is computed.

In Fig. 5 the simulated displacement field and the shear stress for a pristine sample (Fig. 5*a*) consisting of a SiGe island and a Si substrate as well as for samples with a uniform stress of 1, 3 and 5 GPa on the island top facet are presented [Figs. 5(*b*) to 5(*d*)]. For each of these samples a three-dimensional reciprocal-space map was computed from the FEM simulations by FFT and a vertical central cut through the 3D-RSM was performed corresponding to the presentation of experimental data shown in Fig. 4. The calculated 3D-RSM for the pristine sample shows the Si(004) Bragg reflection, the CTR of the Si substrate, and the signal of the SiGe island with the CTRs originating from the side facets of the island. The in-plane epitaxial compressive strain induces a 0.8% Poisson out-of-plane expansion in the pristine island, which results in a displacement of more than 4 nm at the top with respect to the Si reference lattice. This out-of-plane displacement within the island is reduced when an external pressure is applied and becomes negative when the external pressure exceeds 3 GPa, indicating that the lattice parameter of the SiGe island under compression becomes close to that of Si in this direction. Besides the SiGe island, the substrate below the island also exhibits a compressive vertical strain field for large pressures applied on the island top facet resulting in a change of the intensity distribution close to the Si peak. In addition to the displacement field, the deformation of the whole island structure is shown in the top row of Fig. 5. For a better visualization the deformation has been increased by a factor of 25. It shows that the island side facets bend outwards with increasing pressure. This bending of the side facets is caused by a shear stress (see second row of Fig. 5) induced by the pressure application. While a small shear stress exists for the pristine sample, in particular at the island–substrate interface, the absolute value of the shear stress at the side facets increases to more than 1 GPa for an applied pressure of 5 GPa. In reciprocal space this shear stress which causes the bending of the side facets leads to a rotation of CTRs to steeper angles and to change from a straight to a curved line as observed in the calculated 3D-RSMs and the central (q_x, q_z) cuts presented in Figs. 5(*b*)–5(*d*). For visualization, the direction of the CTRs are highlighted by dotted lines drawn by eye along the lines of highest intensity. For the pristine sample, the angle between the facet CTR and the horizontal (⟨110⟩ direction) amounts to 36 ± 2° confirming the value found in the *in situ* experiment (Fig. 4*a*). For ease of comparison, we approximated the curved CTRs for the compressed samples by two parts. One part follows the same angle of 36° as found for the pristine island decreasing in length with increasing pressure; it measures the section of the side plane close to the substrate which is not deformed by mechanical load on top of the island. The second part exhibits a steeper angle increasing to 70° and 80° for an applied pressure of 3 GPa and 5 GPa, respectively. This part clearly measures the deformation of the island top region.

The simulated data are in good qualitative agreement with the experimental ones. According to the calculations, the CTR angle of 60 ± 2° found in the experiment corresponds to an external pressure of ∼2–3 GPa. A detailed analysis of the applied pressure in the experiment is out of the scope of this work. Here, we aimed on the development of a new approach for *in situ* mechanical studies on single submicrometer structures using the SiGe islands as a test structure. As mentioned above, the focal spot of the X-ray beam was smaller than the island. Thus, not all of the SiGe island was illuminated and, hence, the measured diffraction signal may not represent the complete deformation of the specimen. The pressure obtained from the CTR angle is a first estimate of the deformation in the top region of the island. The smaller focal spot size may

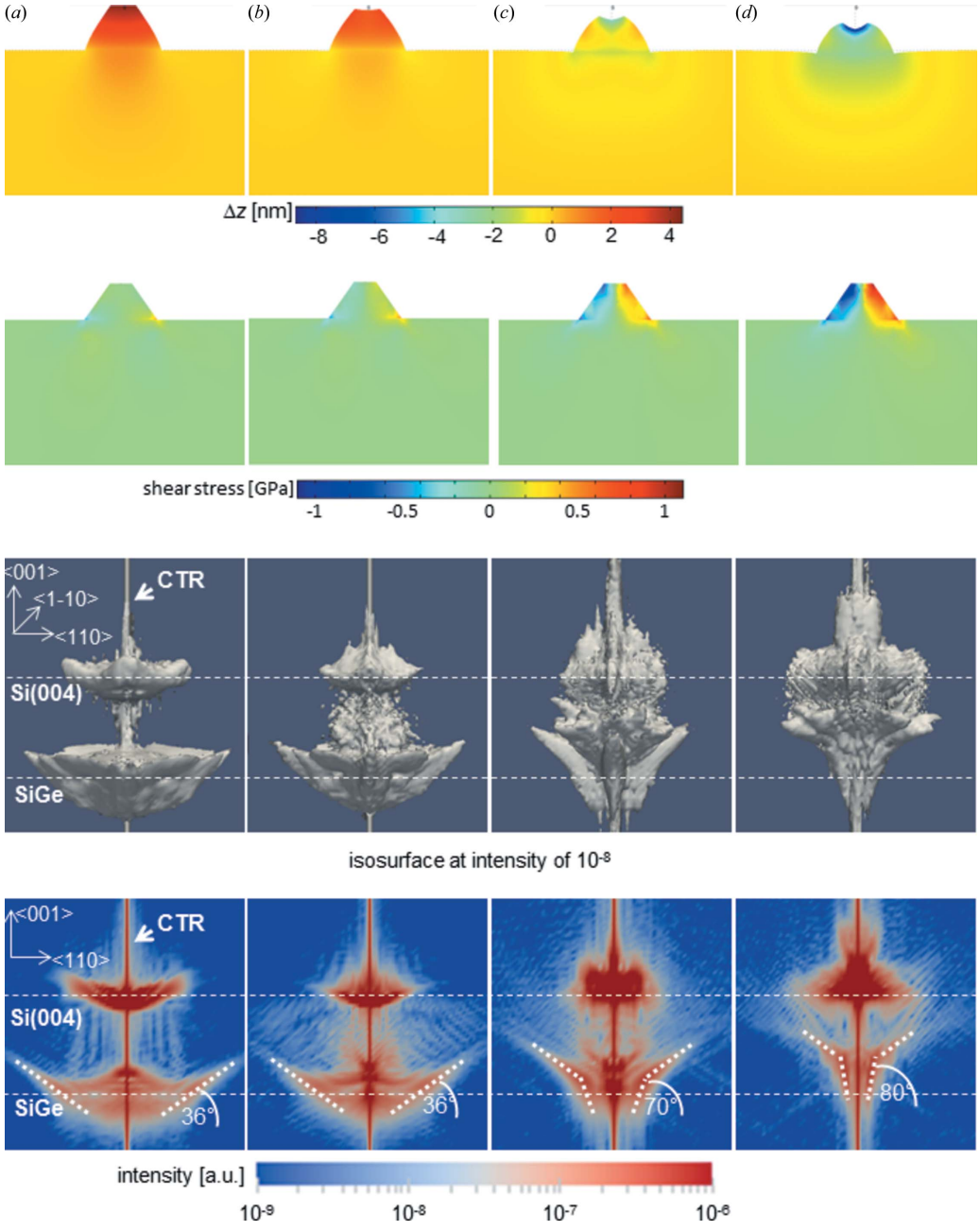

Figure 5
Displacement field (upper row) and shear stress (second row) simulated by the finite-element method using COMSOL's *Multiphysics*, three-dimensional reciprocal-space maps calculated from the displacement fields by fast Fourier transformation (third row), and (q_x, q_z) cuts through the 3D-RSMs at central q_y (fourth row) for (*a*) a SiGe island epitaxically grown on Si(001) and for samples with a distributed load of (*b*) 1 GPa, (*c*) 3 GPa and (*d*) 5 GPa applied on the island top facet. The position of the Si(004) Bragg reflection and the signal of the SiGe island are indicated by dashed lines. The dotted lines highlight the CTRs originating from the island side facets.

also explain differences between the simulated and the measured 3D-RSMs such as a lower diffraction signal in the center of the SiGe island signal or the missing changes close to the Si substrate. This may also be explained by shadowing effects caused by the AFM tip or a deviation of the size or shape of the measured island with respect to the island used in the simulation. Further discrepancies between experiment and simulations may be reduced by considering the inhomogeneous Ge distribution within the island in the calculations. The asymmetry of intensity with respect to $q_x = 0$ found in the experimental diffraction patterns but missing in the simulated ones is attributed to a non-central pressure application with the AFM tip on the island top facet or to a non-central illumination of the island with the X-rays.

4. Conclusions

In conclusion, we showed an *in situ* combination of mechanical loading and three-dimensional reciprocal-space mapping giving access to the deformation of a single submicrometer

structure. Here, we demonstrated this technique by recording *in situ* 3D-RSMs during mechanical compression of a single SiGe island. The data are in good qualitative agreement with simulations based on FEM. The mechanical loading induces a curvature of the island side facets which causes the crystal truncation rods to turn to steeper angles. To our knowledge, this is the first time that the elastic deformation has been recorded for a submicrometer structure *in situ* by three-dimensional reciprocal-space mapping during mechanical testing. This new experimental technique paves the way to novel combinations of *in situ* three-dimensional X-ray diffraction studies and mechanical loading of individual nanostructures for the investigation of their mechanical properties.

The authors gratefully acknowledge the European Synchrotron Radiation Facility (ESRF) in Grenoble (France) for the allocated experiment at the ID01 beamline. We would also like to thank M. Schmidbauer for providing the sample.

References

Benabbas, T., Francois, P., Androussi, Y. & Lefebvre, A. (1996). *J. Appl. Phys.* **80**, 2763–2767.

Biermanns, A., Davydok, A., Paetzelt, H., Diaz, A., Gottschalch, V., Metzger, T. H. & Pietsch, U. (2009). *J. Synchrotron Rad.* **16**, 796–802.

Chen, C. Q., Shi, Y., Zhang, Y. S., Zhu, J. & Yan, Y. J. (2006). *Phys. Rev. Lett.* **96**, 075505.

Christansen, S., Albrecht, M., Strunk, H. P. & Maier, H. J. (1994). *Appl. Phys. Lett.* **64**, 3617–3619.

Cimalla, V., Röhlig, C.-C., Petzoldt, J., Niebelschütz, M., Ambacher, O., Brückner, K., Hein, M., Weber, J., Milenkovic, S., Smith, A. J. & Hassel, A. W. (2008). *J. Nanomater.* **2008**, 638947.

Cornelius, T. W., Carbone, D., Jacques, V. L. R., Schülli, T. U. & Metzger, T. H. (2011). *J. Synchrotron Rad.* **18**, 413–417.

Dorsch, W., Strunk, H. P., Wawra, H., Wagner, G., Groenen, J. & Carles, R. (1998). *Appl. Phys. Lett.* **72**, 179–181.

Favre-Nicolin, V., Mastropietro, F., Eymery, J., Camacho, D., Niquet, Y. M., Borg, B. M., Messing, M. E., Wernersson, L. E., Algra, R. E., Bakkers, E. A. P. M., Metzger, T. H., Harder, R. & Robinson, I. K. (2010). *New J. Phys.* **12**, 035013.

Fewster, P. F. (1997). *Crit. Rev. Solid State*, **22**, 69–110.

Heidelberg, A., Ngo, L. T., Wu, B., Phillips, M. A., Sharma, S., Kamins, T. I., Sader, J. E. & Boland, J. J. (2006). *Nano Lett.* **6**, 1101–1106.

Jefimovs, K., Bunk, O., Pfeiffer, F., Grolimund, D., van der Veen, J. F. & David, C. (2007). *Microelectron. Eng.* **84**, 1467.

Jing, G. Y., Duan, H. L., Sun, X. M., Zhang, Z. S., Xu, J. Li, Y. D., Wang, J. X. & Yu, D. P. (2006). *Phys. Rev. B*, **73**, 235409.

Kiener, D., Grosinger, W., Dehm, G. & Pippan, R. (2008). *Acta Mater.* **56**, 580–592.

Kirchlechner, C., Keckes, J., Micha, J.-S. & Dehm, G. (2011). *Adv. Eng. Mater.* **13**, 837.

Lee, S. W., Jeong, G.-H. & Campbell, E. E. B. (2007). *Nano Lett.* **7**, 2590–2595.

Maaß, R., van Petegem, S., Grollmund, D. & van Swygenhoven, H. (2007). *Appl. Phys. Lett.* **91**, 131909.

Maaß, R., van Petegem, S., Gröllmund, D., van Swygenhoven, H., Kiener, D. & Dehm, G. (2008). *Appl. Phys. Lett.* **92**, 071905.

Mastropietro, F., Carbone, D., Diaz, A., Eymery, J., Sentenac, A., Metzger, T. H., Chamard, V. & Favre-Nicolin, V. (2011). *Opt. Express*, **19**, 19223–19232.

Michler, J., Wasmer, K., Meier, S., Östlund, F. & Leifer, K. (2007). *Appl. Phys. Lett.* **90**, 043123.

Mocuta, C., Stangl, J., Mundboth, K., Metzger, T. H., Bauer, G., Vartanyants, I. A., Schmidbauer, M. & Boeck, T. (2008). *Phys. Rev. B*, **77**, 245425.

Ngo, L. T., Almécija, D., Sader, J. E., Daly, B., Petkov, N., Holmes, J. D., Erts, D. & Boland, J. J. (2006). *Nano Lett.* **6**, 2964–2968.

Östlund, F., Rzepiejewska-Malyska, K., Leifer, K., Hale, L. M., Tang, Y., Ballarini, R., Gerberich, W. W. & Michler, J. (2009). *Adv. Funct. Mater.* **19**, 2439–2444.

Richter, G., Hillerich, K., Gianola, D. S., Mönig, R., Kraft, O. & Volkert, C. A. (2009). *Nano Lett.* **9**, 3048–3052.

Robinson, I. & Harder, R. (2009). *Nat. Mater.* **8**, 291.

Rodrigues, M. S., Cornelius, T. W., Scheler, T., Mocuta, C., Malachias, A., Magalhães-Paniago, R., Dhez, O., Comin, F., Metzger, T. H. & Chevrier, J. (2009). *J. Appl. Phys.* **106**, 103525.

Rodrigues, M. S., Dhez, O., Le Denmat, S., Chevrier, J., Felici, R. & Comin, F. (2008). *J. Instrum.* **3**, 12004.

Sarkar, S. S., Solak, H. H., Raabe, J., David, C. & van der Veen, J. F. (2010). *Microelectron. Eng.* **87**, 854–858.

Scheler, T., Rodrigues, M., Cornelius, T. W., Mocuta, C., Malachias, A., Magalhães-Paniago, R., Comin, F., Chevrier, J. & Metzger, T. H. (2009). *Appl. Phys. Lett.* **94**, 023109.

Smith, D. A., Holmberg, V. C., Lee, D. C. & Korgel, B. A. (2008). *J. Phys. Chem.* C **112**, 10725–10729.

Takagi, S. (1969). *J. Phys. Soc. Jpn*, **26**, 1239–1253.

Uchic, M. D., Dimiduk, D. M., Florando, J. N. & Nix, W. D. (2004). *Science*, **305**, 986–989.

Vegard, L. (1921). *Z. Phys.* **5**, 17–26.

Wang, Z. L., Gao, R. P., Pan, Z. W. & Dai, Z. R. (2001). *Adv. Eng. Mater.* **3**, 657–661.

Wiebach, T., Schmidbauer, M., Hanke, M., Raidt, H., Köhler, R. & Wawra, H. (2000). *Phys. Rev. B*, **61**, 5571–5578.

Wortman, J. J. & Evans, R. A. (1965). *J. Appl. Phys.* **36**, 153–156.